Available online at www.sciencedirect.com
SCIENCE DIRECT®
Acta Materialia 53 (2005) 4029–4041
Acta MATERIALIA
www.actamat-journals.com

Phase stability in the Fe–Ni system: Investigation by first-principles calculations and atomistic simulations

Y. Mishin [a,*], M.J. Mehl [b], D.A. Papaconstantopoulos [a,b]

[a] School of Computational Sciences, George Mason University, Fairfax, VA 22030, USA
[b] Center for Computational Materials Science, Naval Research Laboratory, Washington, DC 20375-5345, USA

Received 6 January 2005; received in revised form 25 April 2005; accepted 3 May 2005
Available online 20 June 2005

Abstract

First-principles calculations of the energy of various crystal structures of Fe, Ni and ordered Fe–Ni compounds with different stoichiometries have been performed by the linearized augmented plane wave (LAPW) method in the generalized gradient approximation. The most stable compounds are $L1_2$–Ni_3Fe, $L1_0$–FeNi, $C11_f$–Ni_2Fe and $C11_f$–Fe_2Ni. The $L1_2$–Ni_3Fe compound has the largest negative formation energy, which is consistent with the experimental Fe–Ni phase diagram. The $L1_0$–FeNi compound has also been observed experimentally in meteorite samples as a metastable phase. It is suggested here that the $C11_f$ compounds could also form in Fe–Ni alloys at low temperatures. A new semi-empirical interatomic potential has been developed for the Fe–Ni system by fitting to experimental data and the results of the LAPW calculations. Recognizing the significance of the covalent component of bonding in this system, the potential is based on the embedded-atom method (EAM) but additionally includes a bond-angle dependence. In comparison with the existing modified EAM method, our potential form is simpler, extends interactions to several (3–5) coordination shells and replaces the screening procedure by a smooth cutoff of the potential functions. The potential reproduces a variety of properties of Fe and Ni with a reasonable accuracy. It also reproduces all stability trends across the Fe–Ni system established by the LAPW calculations. The potential can be useful in atomistic simulations of the phases of the Fe–Ni system.

Keywords: Computer modeling; Interatomic potential; First-principles calculations; Iron; Nickel

1. Introduction

The Fe–Ni system is very important for the understanding of steels and other ferrous alloys, as well as the Earth's core and iron meteorites. Since Ni is a γ-stabilizer in Fe, Fe–Ni alloys offer an ideal model system to study processes in commercial austenitic steels. Fe–Ni alloys are also of interest in connection with the Invar effect and the martensitic transformation from face-centered cubic (fcc) austenite to body-centered cubic (bcc) martensite at low temperatures.

The accepted version of the Fe–Ni phase diagram contains a γ-phase field extending from pure fcc-Fe to pure fcc-Ni, terminal solid solutions based on the bcc α and δ phases of iron, and an intermetallic compound γ′-Ni_3Fe with the $L1_2$ structure [1,2]. In meteorite specimens, a γ″-FeNi phase with the $L1_0$ structure has also been found [3,4]. The precipitation of this phase is only possible under extremely slow (millions of years) cooling conditions that are realized in meteorite alloys and are inaccessible under laboratory conditions. There has been a discussion in the literature as to whether the γ″-phase is stable or metastable [2–4]. The most recent thermodynamic calculations indicate that the γ″-phase is metastable, but it would only take a 300 J/mol (∼0.003 eV/atom) decrease in the free energy to make

* Corresponding author. Tel.: +1 703 993 3984; fax: +1 703 993 1993.
E-mail address: ymishin@gmu.edu (Y. Mishin).

1359-6454/$30.00
doi:10.1016/j.actamat.2005.05.001

this phase stable at room temperature [2]. So far, however, phase stability in the Fe–Ni system has not been studied thoroughly by first-principles calculations or atomistic simulations.

Many properties of Fe–Ni alloys need to be understood at the atomic level. Atomistic computer simulations of dislocation motion [5] and the martensitic transformation [6,7] in this system have been performed with semi-empirical potentials of the embedded-atom method (EAM) [8]. Unfortunately, EAM is not an adequate model for Fe–Ni alloys or even for pure Fe. Although several EAM potentials have been developed for Fe [9–15], their quality remains below the level existing for EAM potentials for simple and noble metals. It has long been recognized that the central-force description of atomic interactions underlying EAM is not accurate for transition metals, particularly for iron. Recently, angular-dependent Fe potentials have been developed using the modified EAM (MEAM) [16,17] and the embedded-defect method (EDM) [13,18–20] and a marked improvement over regular EAM has been demonstrated for a number of properties. It should be pointed out, however, that those angular potentials have been fit to experimental data with little or no input from first-principles calculations.

It has been recognized over recent years that the incorporation of first-principles data in the fitting database significantly improves the reliability of semi-empirical potentials by sampling a larger area of configuration space than experimental data alone can do [21–28]. In the present work we apply this approach, in conjunction with an angular-dependent potential form, to construct a new semi-empirical potential for Fe. As far as Ni is concerned, although it is also a transition metal, it lends itself to an EAM description more readily than Fe (see e.g. [22,28] and references therein). Nevertheless, we wanted to explore whether the incorporation of angular-dependent interactions could further improve the quality of EAM Ni potentials. To address the binary Fe–Ni system, we also use an angular-dependent potential form but its parameters are optimized by fitting to first-principles data only. While particular applications of the potentials developed in this work will be the subject of our future work, in this paper we test their accuracy and transferability by computing a variety of properties of Fe, Ni and Fe–Ni compounds. We place emphasis on the phase stability in the Fe–Ni system, which we study here by both first-principles calculations and with the new interatomic potentials.

In Section 2 of the paper we present the results of first-principles calculations for Fe, Ni and a series of ordered Fe–Ni compounds. In Section 3 we introduce our angular-dependent potential form, followed by a description of the potential parameterization and fitting procedures (Section 4). The potential is tested by calculating properties of Fe (Section 5), Ni (Section 6) and Fe–Ni compounds (Section 7). In Section 8 we summarize our results and draw conclusions.

2. First-principles calculations

The goal of the first-principles calculations conducted in this work is twofold: (1) evaluate the relative stability of different phases of the Fe–Ni system at low temperatures, and (2) generate a database for constructing semi-empirical potentials for this system.

2.1. Methodology

Self-consistent first-principles calculations have been performed for Fe, Ni and ordered Fe–Ni compounds using the full-potential [29] linearized augmented plane wave (LAPW) method [30]. A full relativistic calculation has been made for the core states ($1s^2$, $2s^2$ and $2p^6$) of both Fe and Ni. The spin–orbit interactions [31] for the valence states (including $3s^2$ and $3p^2$ for both elements) are neglected. Local orbitals [32] are used to describe the 3s and 3p levels for both elements. The potentials are calculated using the Perdew–Wang 1991 (PW91) version [33] of the generalized gradient approximation (GGA) to the spin-polarized [34] density functional theory (DFT) [35,36]. It is known that the local density approximation (LDA) overstabilizes the fcc structure of Fe relative to bcc [37] and that one has to use GGA to correctly reproduce bcc-Fe as the ground state [38].

In all of the calculations, we use a muffin-tin radius of $R_{mt} = 2.0$ a.u. for both types of atoms, with a plane-wave cutoff of $K_{max} = 11.5/R_{mt}$. We estimate the error due to this cutoff to be less that 0.5 mRy/atom for the total energy. Integration over the Brillouin zone is implemented using a regular k-point mesh, including the origin, thermal broadening with a temperature of 5 mRy, and extrapolation to zero temperature following Gillan [39]. We have carefully checked the k-point convergence for each structure [40]. For typical fcc-based structures we use a k-point mesh equivalent to 489 points in the irreducible part of the fcc Brillouin zone, while for bcc-based structures we use a mesh of 285 points in the irreducible part of the bcc Brillouin zone. We estimate [41] the integration error due to the finite k-point mesh to be less than 0.1 mRy/atom. In most cases, the magnetic ordering was assumed to be ferromagnetic, i.e., the spin moments of all atoms were aligned in the same direction. In a few cases, however, antiferro- and ferrimagnetic structures were also calculated as explained below (Section 2.2). The computer code used for these calculations was originally written by Krakauer [29,37] and subsequently modified by Singh [32] to implement the local orbital option and by Mehl to include improvements of the GGA option.

The energy of each structure of a metal or compound has been computed for several atomic volumes and the equilibrium lattice parameter has been determined by fitting the energy–volume relation (binding curve) to Birch's equation of state [42]. Non-cubic compounds have been additionally relaxed with respect to the *c/a* ratio.

2.2. LAPW results

For Fe and Ni, the energy–volume functions obtained are in agreement with previous first-principles calculations [7,22,37,38,43–46]. In particular, the loss of magnetic moment of ferromagnetic fcc-Fe under compression produces a double-minimum shape of the binding curve, with non-magnetic fcc-Fe having a larger atomic volume than the ferromagnetic fcc-Fe. The $L1_0$-type antiferromagnetic (AFM) ordering of fcc-Fe (with spin up and down in alternating (200) layers) produces a single-minimum binding curve and reduces the equilibrium energy. The AFM2 ordering (with spins up and down in alternating pairs of adjacent (200) layers) reduces the fcc energy even further, a result which is consistent with previous calculations [7,43–46]. All $Fe_{1-x}Ni_x$ compounds with $x > 0.125$ were treated ferromagnetically. Similarly, we treated the bcc-like cI16 Fe_7Ni compound as ferromagnetic. Treating as ferromagnetic the fcc-like Fe_7Ni compound, which we took to have the Ca_7Ge structure, led to a double-minimum binding curve with both low and high spin minima, just as in fcc-Fe. We then found that we could obtain a lower energy structure by aligning the Ni atom and its six nearest-neighboring Fe atoms with spin in the up direction, and aligning the spin on the remaining Fe atom, which is a second neighbor to the Ni atoms, in the down direction. This ferrimagnetic structure has the usual single-minimum binding curve and does not display a dramatic fall-off in magnetic moment as is seen fcc Fe. This suggests that the magnetic structure of fcc-like low nickel $Fe_{1-x}Ni_x$ compounds might be ferrimagnetic, or, with a large enough unit cell, anti-ferromagnetic.

Table 1 summarizes the equilibrium formation energies, lattice constants and magnetic moments of the Fe–Ni compounds calculated in this work. The formation energy is measured relative to bcc-Fe and fcc-Ni with equilibrium lattice constants. A detailed crystallographic description of the structures can be found at http://cst-www.nrl.navy.mil/lattice/. The stoichiometries of the compounds are chosen so as to cover a wide concentration range from 12.5 to 87.5 at.% Ni. Besides several common structures based on the fcc and bcc lattices, we also include the Ca_7Ge and cI16 structures which represent the fcc and bcc supercells, respectively, with one Ni atom per seven Fe atoms or one Fe atom per seven Ni atoms. These structures are designed to represent atomic environments in dilute solid solutions. Furthermore, grand canonical Monte Carlo simulations with the semi-empirical potential developed in this work (see below) have revealed two more ordered structures that often formed during the simulations at low temperatures (300–400 K). These structures represent stacking sequences of Fe and Ni (002) layers in the fcc lattice: namely, FeFeNiFeFeNi and NiNiFeNiNiFe, respectively. They have the stoichiometries of Fe_2Ni and Ni_2Fe, respectively, and have a conventional unit cell with a triple size in the [001] direction ($a \times a \times 3a$). The subsequent atomic relaxation results in small deviations of the *c/a* ratio from the ideal value of 3. We designate these structures as $C11_f$, in analogy with the bcc-like $C11_b$ ($MoSi_2$ prototype) structure. Since the Monte Carlo simulations have pointed to their high stability, their energy has also been calculated by the LAPW method.

In Fig. 1(a) we plot the composition dependence of the formation energy of the compounds. For structures with multiple magnetic states we include the most stable one. The B1 structure is not shown as its energy lies beyond the scale of this plot. We observe that the addition of Ni to Fe stabilizes fcc-based structures (open circles)

Table 1
Formation energies (per atom, relative to bcc-Fe and fcc-Ni), lattice constants (a_0) and the magnetic moment per atom (M) of Fe–Ni compounds obtained by spin-polarized LAPW/GGA calculations

Formula	Structure	Lattice	Energy (eV)	a_0 (nm)	M (μ_B)
Fe	A2	bcc	0.000	0.2831	2.168
Fe	A1	fcc	0.129	0.3483	1.342
Fe	A1	fcc	0.076	0.3430[a]	0.000[b]
Fe	A1	fcc	0.067	0.3454[c]	0.000[d]
Fe_7Ni	Ca_7Ge	fcc	0.109	0.7029	1.361
Fe_7Ni	Ca_7Ge	fcc	0.092	0.7034	0.942[e]
Fe_7Ni	cI16	bcc	0.009	0.5704	2.244
Fe_3Ni	$L1_2$	fcc	0.048	0.3578	2.066
Fe_3Ni	$D0_3$	bcc	0.034	0.5718	2.162
Fe_2Ni	$C11_f$	fcc	−0.015	0.3525[f]	1.887
FeNi	$L1_0$	fcc	−0.067	0.3556[g]	1.630
FeNi	$L1_1$	fcc	0.002	0.3564	1.588
FeNi	B2	bcc	0.084	0.2854	1.768
FeNi	B1	sc	0.560	0.4745	1.870
Ni_2Fe	$C11_f$	fcc	−0.053	0.3560[h]	1.285
Ni_3Fe	$L1_2$	fcc	−0.089	0.3545	1.202
Ni_3Fe	$D0_3$	bcc	0.024	0.5643	1.102
NiFe	Ca_7Ge	fcc	−0.038	0.7065	0.906
NiFe	cI16	bcc	0.062	0.5628	0.851
Ni	A1	fcc	0.000	0.3519	0.631
Ni	A2	bcc	0.099	0.2801	0.540

The energies and lattice constants of pure Fe and Ni are included for completeness. Unless otherwise indicated, the magnetic state is ferromagnet.

[a] *c/a* = 1.070.
[b] AFM.
[c] *c/a* = 2.172.
[d] AFM2.
[e] Ferrimagnet.
[f] *c/a* = 3.142.
[g] *c/a* = 1.007.
[h] *c/a* = 2.985.

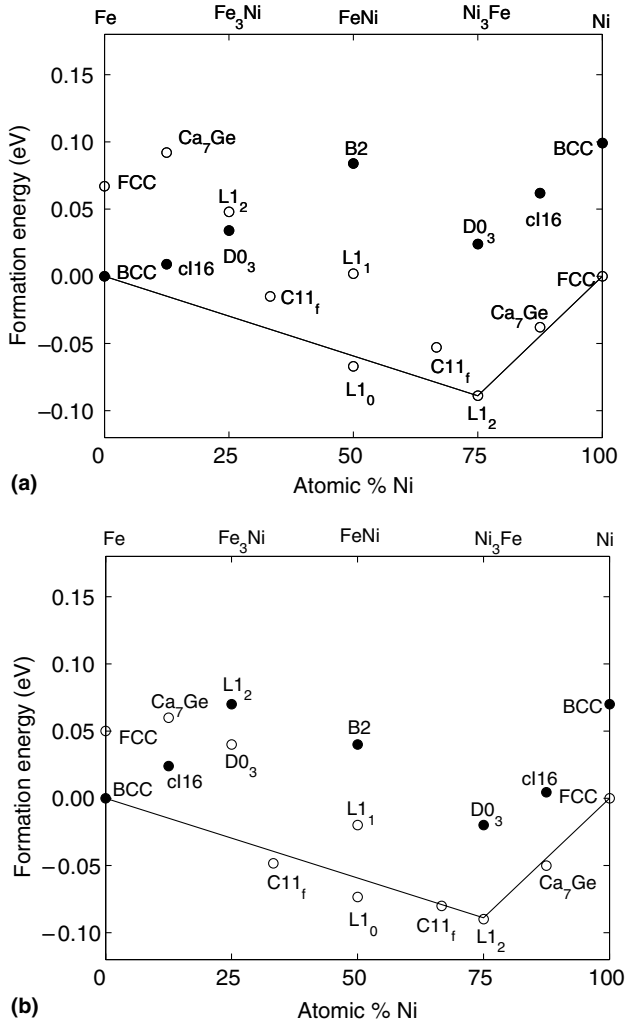

Fig. 1. Formation energies of Fe–Ni compounds relative to bcc-Fe and fcc-Ni obtained by LAPW calculations (a) and with the ADP potential (b). The filled and open symbols represent bcc-type and fcc-type structures, respectively. All structures have been relaxed with respect to atomic volume, and the $L1_0$ and $C11_f$ structures also with respect to the *c/a* ratio. The lines show the tie lines corresponding to the experimental phase diagram.

and destabilizes bcc-based structures (filled circles), a trend which is consistent with the experimental phase diagram [1]. We also observe that the $L1_2$–Ni_3Fe phase, which is present on the experimental diagram, has the most negative formation energy out of all compounds calculated in this work. According to the experimental phase diagram, the formation energies of all alternate phases should lie above the tie lines connecting $L1_2$–Ni_3Fe with bcc-Fe and fcc-Ni. Furthermore, phases whose formation energies are closer to these tie lines are most stable and have a greater chance to be found in experiments under metastable conditions.

In agreement with experimental observations of the $L1_0$–FeNi (γ'') phase [2–4,47], its formation energy lies practically on a tie line. Actually, it lies even slightly below the tie line, but the energy difference ($\sim$0.01 eV) is comparable to the accuracy of our calculations. Even if the LAPW energy of $L1_0$–FeNi lies slightly below the tie line at 0 K, the situation can be reversed at finite temperatures due to the effect of atomic vibrations. Already the energy of zero-point vibrations, ε_0, can readily exceed 0.01 eV. Indeed, assuming that the Debye temperatures θ of the relevant phases (bcc-Fe, $L1_0$–FeNi and $L1_2$–Ni_3Fe) are close to room temperature (in reality they are higher), ε_0 equals approximately $k_B\theta/2 \sim 0.013$ eV, k_B being Boltzmann's constant. Since ε_0 values of the phases are generally different, it is quite possible for them to shift the formation energy of $L1_0$–FeNi by an amount comparable to 0.01 eV. At finite temperatures, the normal atomic vibrations can produce an even stronger effect on the free energies. Our calculations are, therefore, consistent with the experimentally observed high stability of the γ''-phase despite its absence on the accepted version of the phase diagram. Our results are also compatible with the thermodynamic calculations [2] predicting a slight (0.003 eV) metastability of this phase at room temperature.

Finally, in agreement with predictions of our Monte Carlo simulations discussed below, the LAPW formation energies of the $C11_f$ compounds are relatively low, lying near the Fe–Ni_3Fe tie line. This allows us to make a prediction that these structures could actually form in Fe–Ni alloys at low temperatures as metastable phases.

3. The angular-dependent potential method

To enable atomistic simulations of the Fe–Ni system, we need a semi-empirical potential that incorporates the covalent component of bonding in this system and builds on both first-principles and experimental data. To this end, we propose a potential form that generalizes EAM by including angular-dependent interactions. It is inspired by the MEAM [16,48–50] and EDM [18] methods but is different from them in certain aspects. To reflect this distinction, we refer to our potential form as the *Angular-Dependent Potential* (ADP) method. In this method, the total energy E_{tot} of a collection of atoms is defined by the following expression in an orthogonal Cartesian system:

$$E_{\text{tot}} = \frac{1}{2}\sum_{i,j(j\neq i)} \Phi_{s_i s_j}(r_{ij}) + \sum_i F_{s_i}(\bar{\rho}_i) + \frac{1}{2}\sum_{i,\alpha}(\mu_i^\alpha)^2 + \frac{1}{2}\sum_{i,\alpha,\beta}(\lambda_i^{\alpha\beta})^2 - \frac{1}{6}\sum_i v_i^2. \quad (1)$$

Here indices i and j enumerate atoms and the superscripts $\alpha, \beta = 1, 2, 3$ refer to the Cartesian directions. The first term in Eq. (1) represents pair interactions between atoms, $\Phi_{s_i s_j}(r_{ij})$ being the pair-interaction potential between an atom i of chemical sort s_i located at

position $\mathbf{r}_i$ and an atom j of chemical sort s_j at position $\mathbf{r}_j = \mathbf{r}_i + \mathbf{r}_{ij}$. The function F_{s_i} is the embedding energy of atom i in the host electron density $\bar{\rho}_i$ induced at site i by all other atoms of the system. The host electron density is given by

$$\bar{\rho}_i = \sum_{j\neq i} \rho_{s_j}(r_{ij}), \tag{2}$$

where $\rho_{s_j}(r)$ is the electron density function assigned to an atom j. The second term in Eq. (1) was introduced in EAM [8] and represents many-body interactions between atoms. Thus, the first two terms in Eq. (1) constitute the regular EAM potential form [8]. Notice that they have a central-force character, i.e., depend on the interatomic distances r_{ij} only and not on bond angles. The following three terms in Eq. (1) introduce non-central components of bonding through the vectors

$$\mu_i^\alpha = \sum_{j\neq i} u_{s_i s_j}(r_{ij}) r_{ij}^\alpha \tag{3}$$

and tensors

$$\lambda_i^{\alpha\beta} = \sum_{j\neq i} w_{s_i s_j}(r_{ij}) r_{ij}^\alpha r_{ij}^\beta. \tag{4}$$

The quantities v_i are traces of the λ-tensor:

$$v_i = \sum_\alpha \lambda_i^{\alpha\alpha}. \tag{5}$$

In Eqs. (3) and (4), $u_{ss'}(r)$ and $w_{ss'}(r)$ are two additional pairwise functions introduced in this method, which depend on the interatomic distance r and the chemical sorts s and s'. The quantities μ_i^α and $\lambda_i^{\alpha\beta}$ can be thought of as measures of the dipole and quadrupole distortions, respectively, of the local environment of atom i. As in the MEAM and EDM methods, the role of the angular terms is to penalize the total energy for deviations of the atomic environments from cubic symmetry. While these terms vanish in a perfect cubic structure regardless of its volume, they turn on under non-hydrostatic strains and thus affect the elastic constants of both cubic and non-cubic crystals. These terms are especially important in non-centrosymmetric structures (such as diamond and HCP) and in materials with a negative Cauchy pressure. The angular terms are essential for modeling bcc transition metals as they capture, in a semi-empirical manner, the covalent component of bonding existing in such materials. In binary compounds, the angular terms affect the energy of such common structures as $L1_0$, $L1_1$ and even $L1_2$, but vanish in the B1 and B2 structures. Since most lattice defects in materials break the local lattice symmetry, the defect formation energies are also affected by the angular terms.

In MEAM [16,48–50], angular-dependent interactions are also introduced through dipole, quadrupole and higher-order multipoles similar to Eqs. (3)–(5). However, in MEAM they constitute a part of the tensor electron density whereas in the ADP method they contribute to E_{tot} directly. Our Eq. (1) can formally be derived from the MEAM formalism by applying a linear expansion of the embedding energy in terms of the invariants of the dipole and quadrupole contributions to the electron density and neglecting all higher-order terms. Furthermore, MEAM normally restricts interactions to one or two coordination shells and introduces a many-body screening procedure. In contrast, ADP functions extend to as many coordination shells as necessary (usually, 3–5) and replace the screening procedure by a smooth cutoff similar to regular EAM. This makes the energy and force computations in ADP simpler and faster than in MEAM. In addition, due to the closer similarity between the EAM and ADP methods, an implementation of ADP potentials in an existing atomistic simulation code may require less coding effort. ADP simulations run approximately a factor of two slower than EAM simulations. Expressions for the forces on atoms within the ADP method are given in Appendix. These expressions are needed for both the energy minimization and molecular dynamics simulations with ADP potentials.

The EDM has only been formulated for monatomic systems [18] and represents a particular case of the ADP method. To obtain the EDM potential form from ADP, one should consider a monatomic system, neglect the dipole term in Eq. (1) and replace the quadrupole function $w(r)$ by $Y\rho(r)$, where $\rho(r)$ is the scalar electron density defined by Eq. (2) and Y is a parameter. Thus, EDM offers only one adjustable parameter to control all angular-dependent interactions. The neglect of the dipole term can be disadvantageous when calculating elastic constants and phonon frequencies in non-centrosymmetric structures and in simulations of lattice defects in transition metals.

An ADP description of a pure metal requires five functions: $\Phi(r)$, $\rho(r)$, $F(\bar{\rho})$, $u(r)$ and $w(r)$ (compare with three functions in EAM). For a binary system A–B we need 13 functions: $\Phi_{AA}(r)$, $\Phi_{BB}(r)$, $\Phi_{AB}(r)$, $\rho_A(r)$, $\rho_B(r)$, $F_A(\bar{\rho})$, $F_B(\bar{\rho})$, $u_{AA}(r)$, $u_{BB}(r)$, $u_{AB}(r)$, $w_{AA}(r)$, $w_{BB}(r)$ and $w_{AB}(r)$ (compare with seven functions in EAM). A reasonable approach to generating a binary ADP potential is to first construct elemental ADP potentials for metals A and B and then fit the cross-interaction functions $\Phi_{AB}(r)$, $u_{AB}(r)$ and $w_{AB}(r)$. This approach is applied to the Fe–Ni system.

4. ADP parameterization and fitting

4.1. Parameterization of potential functions

For the elemental bcc-Fe and fcc-Ni, the electron density function is chosen in the form

$$\rho(r) = \psi\left(\frac{r - r_c}{h}\right)[A_0 z^y \mathrm{e}^{-\gamma z}(1 + B_0 \mathrm{e}^{-\gamma z}) + C_0], \tag{6}$$

where $z = r - r_0$ and $\psi(x)$ is a cutoff function defined by

$$\psi(x) = \frac{x^4}{1 + x^4} \tag{7}$$

if $x < 0$ and $\psi(x) \equiv 0$ if $x \geqslant 0$. Eq. (6) parameterizes $\rho(r)$ with fitting parameters B_0, C_0, r_0, y, γ, r_c and h. The coefficient A_0 is adjusted to give a unit host electron density for the equilibrium lattice parameter. The pair interaction potential is postulated in the form of a generalized Lennard–Jones function

$$\Phi(r) = \psi\left(\frac{r - r_c}{h}\right)\left[\frac{V_0}{b_2 - b_1}\left(\frac{b_2}{z^{b_1}} - \frac{b_1}{z^{b_2}}\right) + \delta\right] + m\rho(r), \tag{8}$$

where $z = r/r_1$, with fitting parameters b_1, b_2, r_1, V_0, δ and m. We found it useful to admix to $\Phi(r)$ the electron density $\rho(r)$ with an adjustable weight m. This mixing provides more flexibility in optimizing the shape of $\Phi(r)$. The cutoff function guarantees that both $\rho(r)$ and $\Phi(r)$ as well as their derivatives up to the second one turn smoothly to zero at a common cutoff distance r_c.

The embedding energy $F(\bar{\rho})$ is obtained by inverting the universal equation of state, which we postulate in the form [27,28,51]

$$E(a) = E_0\left[1 + \alpha x + \beta\alpha^3 x^3 \frac{2x + 3}{(x + 1)^2}\right]\mathrm{e}^{-\alpha x}. \tag{9}$$

Here $x = a/a_0 - 1$,

$$\alpha = \left(-\frac{9\Omega_0 B}{E_0}\right)^{1/2},$$

E is the crystal energy per atom relative to a set of isolated atoms, E_0 is the equilibrium cohesive energy (minimum value of E), a is the cubic lattice parameter, a_0 is the equilibrium value of a, Ω_0 is the equilibrium atomic volume, B is the bulk modulus and β is a parameter. The latter can be adjusted to the experimental high-pressure behavior of a metal as it was done in [27]. In this work, however, we choose $\beta = 0$ for Fe (experimental data extending over a wide enough range of pressures are not available) and reuse the value $\beta = 4.89 \times 10^{-3}$ from our previous EAM potential for Ni [28]. Notice that the inversion of Eq. (9) guarantees an exact fit to a_0, E_0 and B.

The dipole and quadrupole functions are parameterized by exponents,

$$u(r) = \psi\left(\frac{r - r_c}{h}\right)(d_1 \mathrm{e}^{-d_2 r} + d_3), \tag{10}$$

$$w(r) = \psi\left(\frac{r - r_c}{h}\right)(q_1 \mathrm{e}^{-q_2 r} + q_3), \tag{11}$$

q_i and d_i being fitting parameters. Both functions are subject to the same cutoff as $\rho(r)$ and $\Phi(r)$.

The cross-interaction function $\Phi_{\mathrm{FeNi}}(r)$ is chosen in the form of a mixture of the pair-interaction functions of Fe and Ni with exponential weights,

$$\Phi_{\mathrm{FeNi}}(r) = t_1 \mathrm{e}^{-t_2 r}\Phi_{\mathrm{Fe}}(r) + t_3 \mathrm{e}^{-t_4 r}\Phi_{\mathrm{Ni}}(r), \tag{12}$$

with four parameters t_i. The cross dipole and quadrupole functions are chosen as mixtures of the relevant elemental functions,

Table 2
Optimized values of fitting parameters of the ADP potentials for Fe, Ni and Fe–Ni

Fe		Ni		Fe–Ni	
Parameter	Value	Parameter	Value	Parameter	Value
r_c (nm)	0.5055	r_c (nm)	0.5168	t_1	0.4349
h_c (nm)	0.6202	h_c (nm)	0.3323	t_2 (nm)	−2.2375
V_0 (eV)	-3.5674×10^4	V_0 (eV)	-3.5126×10^3	t_3	0.2432×10^{-1}
r_1 (nm)	0.1769	r_1 (nm)	3.8673×10^{-5}	t_4 (nm)	−8.9329
b_1	5.4824×10^{-2}	b_1	4.7067×10^{-3}	m_q	0.8817
b_2	7.7124	b_2	0.1511	m_d	1.3189×10^{-2}
δ (eV)	3.6665×10^4	δ (eV)	3.6046×10^3	s_{Ni}	0.5780
m (eV)	7.0735×10^2	m (eV)	0.0000	g_{Fe} (eV)	−2.0833
y	2.0201×10^1	y	1.9251×10^1	g_{Ni} (eV)	−2.5435
γ (1/nm)	1.2981×10^1	γ (1/nm)	1.6802×10^1		
B_0	1.1171×10^5	B_0	1.1914×10^5		
C_0	0.1391	C_0	0.2033		
r_0 (nm)	−0.4052	r_0 (nm)	−0.3138		
β	0.0000	β	0.4890×10^{-2}		
d_1 (eV$^{1/2}$/nm)	1.9135	d_1 (eV$^{1/2}$/nm)	4.4657×10^{-2}		
d_2 (1/nm)	-1.0796×10^1	d_2 (1/nm)	-1.3702×10^1		
d_3 (eV$^{1/2}$/nm)	−0.8928	d_3 (eV$^{1/2}$/nm)	−0.9611		
q_1 (eV$^{1/2}$/nm^2)	−5.8954	q_1 (eV$^{1/2}$/nm^2)	6.4502×10^2		
q_2 (1/nm)	-1.3872×10^1	q_2 (1/nm)	0.2608		
q_3 (eV$^{1/2}$/nm^2)	2.4790×10^2	q_3 (eV$^{1/2}$/nm^2)	-6.0208×10^2		

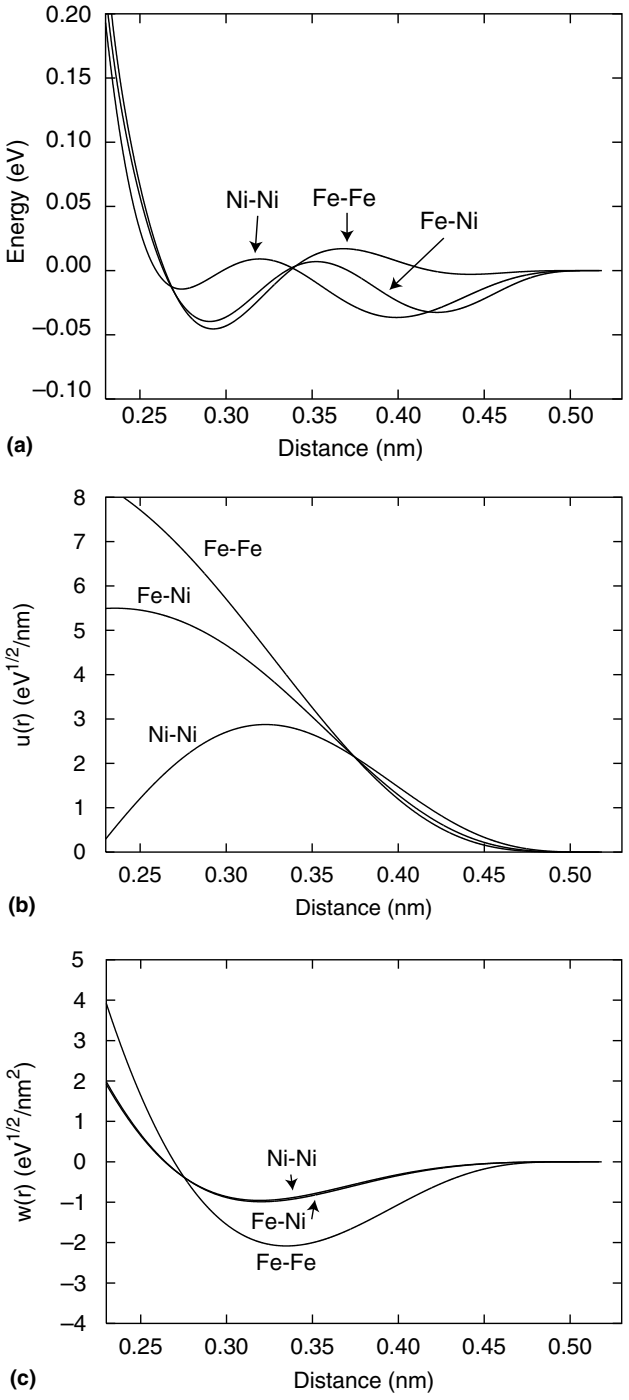

Fig. 2. ADP potential functions: (a) pair interaction functions $\Phi(r)$, (b) dipole functions $u(r)$, (c) quadrupole functions $w(r)$.

$$u_{\mathrm{FeNi}}(r) = (1 - m_{\mathrm{d}})u_{\mathrm{Fe}}(r) + m_{\mathrm{d}}u_{\mathrm{Ni}}(r), \quad (13)$$

$$w_{\mathrm{FeNi}}(r) = (1 - m_{\mathrm{q}})w_{\mathrm{Fe}}(r) + m_{\mathrm{q}}w_{\mathrm{Ni}}(r), \quad (14)$$

with adjustable weights m_{d} and m_{q}. The potential transformation coefficients s_{Ni}, g_{Fe} and g_{Ni} (see e.g. [25,27,28,52] for their definition) are also used as adjustable parameters. The particular analytical forms of the potential function defined by Eqs. (6)–(14) were obtained by trying a number of different forms and selecting those which provided the best quality of fit with less parameters.

4.2. Fitting database

For Fe and Ni, the fitting database includes experimental values of a_0, E_0, three elastic constants c_{ij}, the vacancy formation ($E_{\mathrm{v}}^{\mathrm{f}}$) and migration ($E_{\mathrm{v}}^{\mathrm{m}}$) energies, and the surface energy γ_{s}. We choose one particular surface orientation for each metal and fit its energy to the experimental orientation-averaged surface energy. The database also includes LAPW energy–volume relations for the fcc, bcc, simple cubic (sc) and diamond-cubic structures. The Ni fit additionally includes the HCP and $L1_2$ structures, the latter being a defected fcc structure with one unrelaxed vacancy per cubic unit cell. The Fe–Ni binary fit is based on first-principles data only. Namely, we use LAPW energy–volume relations for the following Fe–Ni compounds: $L1_2$–Fe_3Ni, $D0_3$–Fe_3Ni, $L1_0$–FeNi, $L1_1$–FeNi, B1–FeNi, B2–FeNi, $L1_2$–Ni_3Fe and $D0_3$–Ni_3Fe. Several other compounds discussed in Section 2 are used for testing the potential.

The potential functions have been optimized by minimizing the weighted mean-squared deviation of properties from their target values by a simulated annealing method. For Fe, the optimized $\Phi(r)$ was subsequently modified by adding a function $27(r - r_*)^4$ at $r < r_* = 0.244$ nm to eliminate an unphysical feature that existed at short separations. For Ni, we retain all EAM functions constructed in [28] and only adjust angular-dependent interactions. This gives us an opportunity to explore the extent to which angular terms can improve an existing EAM potential. The optimized parameters are reported in Table 2 and are illustrated in Fig. 2. Tabulated forms of the functions are available via the World Wide Web at http://cst-www.nrl.navy.mil/bind/eam or from the authors by request.

5. ADP results for Fe

The ADP cohesive energies of alternate structures of Fe are in reasonable agreement with the respective LAPW energies determined by the Birch fit [42] (Table 3). For fcc-Fe, the potential predicts the lattice

Table 3
Equilibrium energies (in eV) of alternative structures of Fe and Ni relative to the ground state obtained with the ADP potential and by the present first-principles LAPW calculations

Structure	Fe		Ni	
	LAPW	ADP	LAPW	ADP
fcc	0.07	0.05	0.00	0.00
bcc	0.00	0.00	0.10	0.07
sc	0.75	0.61	1.00	0.72
Diamond	1.23	1.29	1.94	1.42

Table 4
Properties of bcc-Fe calculated with the ADP potential in comparison with experimental data, first-principles and tight-binding (TB) calculations

Property	Experiment	Ab initio/TB	ADP
a_0 (nm)*	0.28665[a]		0.28665
E_0 (eV)*	−4.28[a]		−4.30
c_{11} (GPa)*	242.0[b]	250.0[c]	254.9
c_{12} (GPa)*	146.5[b]	145.0[c]	140.0
c_{44} (GPa)*	112.0[b]	142.0[c]	121.5
α (10^{-6}/K)	11.8[d]		14.9
T_m (K)	1811[a]		2135
E_v^f (eV)*	2.0 ± 0.2[e]	1.93–2.02[f]; 2.07[g]; 2.35[c]	2.13
E_v^m (eV)*	0.91[h]; 0.55[i]	0.65[f]; 0.67[g]	0.74
E_i^f [1 0 0] (eV)		4.37[f]; 4.64[g]	4.00
E_i^f [1 1 0] (eV)		3.41[f]; 3.64[g]	3.48
E_i^f [1 1 1] (eV)		4.11[f]; 4.34[g]	3.23
γ_{us} (J/m^2)		0.47[j]; 0.59[k]	0.600
γ_s (1 0 0) (J/m^2)	2.360[l]	2.179[m]	2.174
γ_s (1 1 0) (J/m^2)	2.360[l]		2.177
γ_s (1 1 1) (J/m^2)*	2.360[l]		2.446

The properties marked by an asterisk were included in the potential fit. The notation of properties is explained in the text.

[a] Ref. [53].
[b] Ref. [75].
[c] Ref. [63]
[d] Ref. [76].
[e] Ref. [54].
[f] Ref. [58].
[g] Refs. [59,60].
[h] Deduced from $E_v^f = 2.0 \pm 0.2$ eV [54] and the activation energy of self-diffusion 2.91 ± 0.04 eV, Refs. [56,57].
[i] Ref. [55].
[j] Spin-polarized GGA, Ref. [64].
[k] Spin-polarized LDA, Ref. [64].
[l] For average orientation, Ref. [71].
[m] Ref. [14].

parameter $a_0 = 0.36032$ nm and the cohesive energy $E_0 = -4.2498$ eV. This phase is mechanically unstable with a negative shear modulus ($c_{11} < c_{12}$).

Table 4 summarizes properties of bcc-Fe computed with the ADP potential in comparison with experimental data and first-principles calculations. The lattice parameter $a_0 = 0.28665$ nm and the cohesive energy $E_0 = -4.30$ eV are fit to the target values exactly.[1] The elastic constants are accurately fit to the experimental values. The vacancy formation and migration energies are in good agreement with both experimental data [54–57] and first-principles calculations [58–60]. The vacancy migration energy has been computed by the nudged elastic band (NEB) method [61,62]. The energy along the reaction coordinate of a vacancy jump shows only one maximum occurring at the midpoint (1/2)[1 1 1], which is consistent with first-principles calculations [60]. In contrast, some of the previous potentials [12,14] produce a double-hump energy profile with a distinct local minimum at (1/2)[1 1 1]. This is apparently an artifact of those potentials. The activation energy of self-diffusion by the vacancy mechanism, $E_v^f + E_v^m = 2.87$ eV, is in excellent agreement with direct experimental measurements, 2.91 ± 0.04 eV [56,57].

The self-interstitial formation energies (E_i^f) have been computed for three different split-dumbbell orientations (Table 4). While the energies of the [1 0 0] and [1 1 0] orientations compare well with first-principles [58,59] and tight-binding [63] calculations, the potential clearly overstabilizes the [1 1 1] dumbbell. The origin of this discrepancy is in a large lattice relaxation accompanying the formation of this dumbbell, with significant atomic displacements along the [1 1 1] direction. We notice that interstitial formation energies were not included in the potential fit. Semi-empirical potentials often have problems reproducing the correct ordering of E_i^f values in bcc metals. As a general trend, short-range potentials correctly predict the [1 1 0] dumbbell to be the ground state whereas long-range potentials favor a delocalized [1 1 1] dumbbell [13]. The latter was apparently the case with our potential. The unstable stacking fault energy γ_{us} has been calculated by applying shear deformation along the $[1\bar{1}1](1\,1\,0)$ path and is consistent with

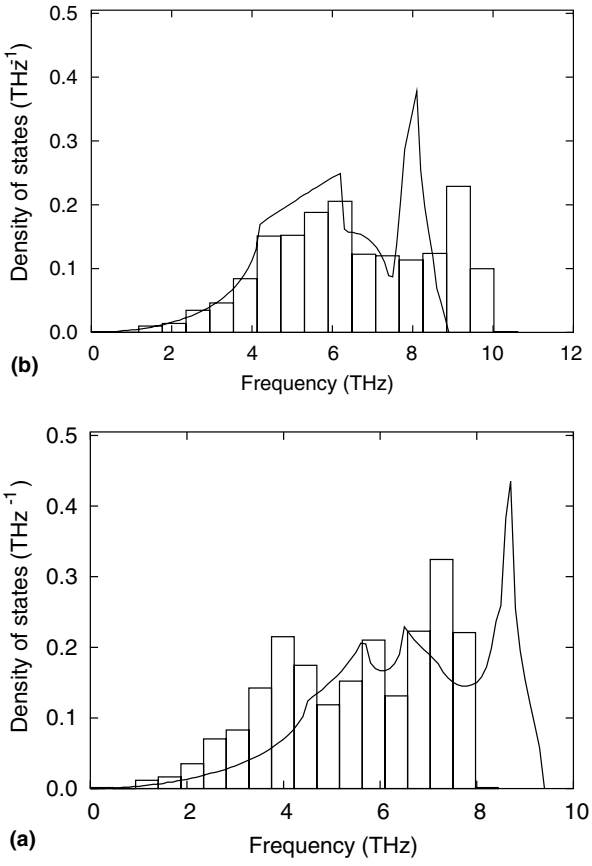

Fig. 3. Phonon density of states of (a) bcc-Fe and (b) fcc-Ni measured experimentally at 296 K (lines) [65] and calculated with the ADP potentials at 0 K (bars).

[1] While the literature value is $E_0 = -4.28$ eV [53], we found that the choice of $E_0 = -4.30$ eV allows a slightly better fit to other properties.

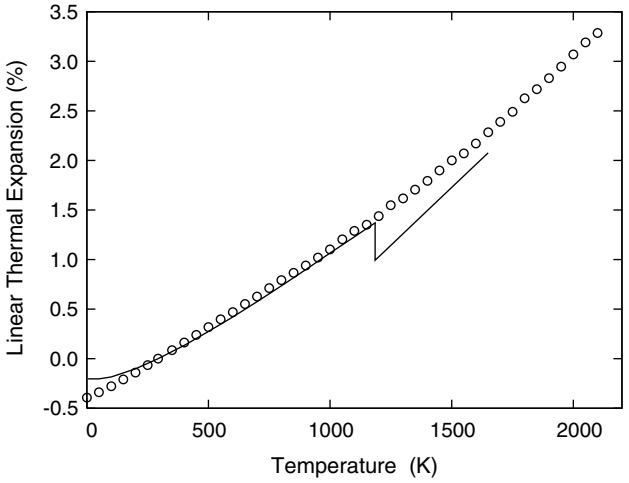

Fig. 4. Linear thermal expansion factor of bcc-Fe relative to room temperature (293 K) computed with the ADP potential (points) by NPT Monte Carlo simulation. The experimental data (lines) are the 'recommended' values from [76]. The break in the experimental data is due to the bcc-fcc phase transformation.

first-principles calculations [64]. The surface energies are in very good agreement with experiment, and for the (1 0 0) orientation, also with the recent first-principles calculation [14].

The phonon density of states (DOS) at 0 K has been estimated by diagonalizing the dynamical matrix of a $9\times9\times9$ (1458 atoms) periodic supercell and calculating the distribution of the normal vibrational frequencies over 15 frequency intervals from zero to the maximum frequency. The result is shown in Fig. 3 as a bar diagram in comparison with the experimental DOS measured at 296 K [65]. While the shape of the DOS predicted by the potential is qualitatively correct, all frequencies are scaled 15% down with respect to the experiment. The thermal expansion factor α at room temperature is in good agreement with experiment. Fig. 4 illustrates the temperature dependence of the linear thermal expansion coefficient over a wide temperature range. The melting temperature of Fe has been computed by molecular dynamics simulations using the solid–liquid interface method. The value obtained, $T_m = 2135$ K, overestimates the experimental melting point 1811 K. Other Fe potentials give $T_m = 2358$ K [12], 2060 K [17] and 1772 K [14]. In the latter case, however, liquid properties were included in the fit.

6. ADP results for Ni

The Ni structural energies calculated with the ADP potential are in reasonable agreement with the LAPW energies (Table 3). Table 5 compares ADP properties of fcc-Ni with experimental data and with calculations

Table 5
Properties of fcc-Ni calculated with the ADP potential in comparison with the EAM potential [28] and experimental data

Property	Experiment	ADP	EAM
a_0 (nm)*	0.352[a]	0.352	0.352
E_0 (eV)*	−4.45[a]	−4.45	−4.45
c_{11} (GPa)*	246.5[b]	242.4	241.3
c_{12} (GPa)*	147.3[b]	150.3	150.8
c_{44} (GPa)*	124.7[b]	129.6	127.3
α (10^{-6}/K)	13.4[c]	7.9	8.3
T_m (K)	1728[a]	1805	1715
E_v^f (eV)*	1.60[d]	1.63	1.57
E_v^m (eV)*	1.30[e]	1.34	1.19
E_i^f [1 0 0] (eV)		4.92	4.71
E_i^f [1 1 0] (eV)		4.82	4.58
E_i^f [1 1 1] (eV)		4.70	4.49
γ_{SF} (J/m^2)	0.128[f]	0.136	0.134
γ_{us} (J/m^2)		0.303	0.298
γ_s (1 0 0) (J/m^2)	2.280[g]	2.172	1.936
γ_s (1 1 0) (J/m^2)*	2.280[g]	2.329	2.087
γ_s (1 1 1) (J/m^2)	2.280[g]	2.005	1.759

The properties marked by an asterisk were included in the potential fit. The notation of properties is explained in the text.

[a] Ref. [53].
[b] Ref. [77].
[c] Ref. [76].
[d] Refs. [66].
[e] Ref. [67].
[f] Ref. [69].
[g] For average orientation, Refs. [69,71].

using the EAM potential [28]. Both the ADP and EAM potentials are fit accurately to the experimental elastic constants and the vacancy formation and migration energies [66,67]. The activation energies of self-diffusion, $E_v^f + E_v^m = 2.97$ eV (ADP) and 2.76 eV (EAM), compare well with experimental data (2.88 eV [68]), the ADP value being slightly more accurate. The self-interstitial formation energies have been computed for three different split-dumbbell orientations and the [1 1 1] orientation has been found to be the most stable. The intrinsic stacking fault energy γ_{SF} is in good agreement with experimental data (0.128 J/m^2 [69]) and first-principles calculations (0.145 J/m^2 [70]). The unstable stacking fault energy calculated along the $[\bar{2}\,1\,1](1\,1\,1)$ path compares reasonably well with first-principles calculations (0.269 J/m^2 [70]). The ADP surface energies are in very good agreement with experiment [69,71]. They also compare very well with first-principles calculations, which give 2.19, 2.35 and 1.93 J/m^2 for the (1 0 0), (1 1 0) and (1 1 1) orientations, respectively [72]. In contrast, the EAM potential underestimates the surface energies, which reflects the common problem of EAM potentials. The improvement in the surface energies is due to the angular-dependent interactions included in the ADP potential.

The phonon DOS at 0 K has been calculated by diagonalizing the dynamical matrix of a $7\times7\times7$ (1372 atoms) supercell and constructing a distribution

of the normal vibrational frequencies. In comparison with the experimental DOS measured at 293 K [65] (Fig. 3), the shape of the DOS predicted by the ADP potential is qualitatively correct but the high-frequency peak is smeared and shifted towards higher frequencies. The melting temperature of Ni computed by molecular dynamics simulations is reasonably close to the experimental value, especially with the EAM potential. The ADP thermal expansion coefficient is close to that calculated with the EAM potential but both coefficients underestimate the experiment. Thermal expansion was not included in the ADP fit but was used, with a small weight, when constructing the EAM potential [28]. Overall, despite some improvement in the vacancy migration energy and in surface energies, the incorporation of angular-dependent interactions has not led to a drastic improvement over the existing EAM Ni potential [28]. This confirms the notion that Ni can be adequately described by regular EAM [28]. For the sake of consistency, our Fe–Ni potential set is based on the new ADP Ni potential.

7. ADP results for Fe–Ni compounds

The equilibrium formation energies of the Fe–Ni compounds computed with the ADP potential are compared with their LAPW counterparts in Fig. 1. The B1–FeNi formation energy lies far beyond the scale of these plots, but the agreement between the respective ADP (0.55 eV) and LAPW (0.56 eV) energies is excellent. Recall that only some of these compounds were used in the ADP fit (Section 4) while the energies of the other compounds are predictions of the potential. The agreement between the LAPW and ADP calculations is very good. Both calculation methods identify the same set of compounds that are most stable and tend to group around the tie lines, namely, $C11_f$–Fe_2Ni, $L1_0$–FeNi, $L1_2$–Ni_3Fe, $C11_f$–Ni_2Fe and Ni_7Fe. The high stability of $L1_0$–FeNi is consistent with experimental observations of this phase in meteorite samples [2–4,47]. Furthermore, both calculations predict that the $C11_f$–compounds Fe_2Ni and Ni_2Fe could also be observed at low temperatures. Note also that the formation energy of Ni_7 Fe with the fcc-based Ca_7Ge structure is also very low (lies on the Ni_3Fe–Ni tie line in both LAPW and ADP calculations), which is consistent with the high solubility of Fe in fcc-Ni. This compound was not included in the ADP fit.

Table 6 demonstrates that lattice properties of $L1_2$–Ni_3Fe predicted by the ADP potential compare very well with experimental data. Given the fact that no experimental data were used for fitting the Fe–Ni interactions, this agreement points to a good transferability of the potential.

Table 6
Properties of $L1_2$–Ni_3Fe calculated with the ADP potential in comparison with experimental data

Property	Experiment	ADP
a_0 (nm)	0.3555[a]	0.35627
E_0 (GPa)		−4.5065
c_{11} (GPa)	230.4[b]	233.7
c_{12} (GPa)	144.4[b]	155.7
c_{44} (GPa)	119.2[b]	122.8

[a] Refs. [47,78].
[b] Ref. [77].

8. Discussion and conclusions

First-principles LAPW calculations have been performed for a variety of crystal structures of Fe, Ni and ordered Fe–Ni compounds. The $L1_2$–Ni_3Fe compound has the largest negative formation energy (Fig. 1) in comparison with all other compounds calculated in this work. This result is consistent with the experimental phase diagram, which contains the γ-phase based on this compound in equilibrium with bcc-Fe and fcc-Ni at temperatures below 620 K [1]. The formation energy of another important compound, $L1_0$–FeNi, lies practically on the tie line connecting Ni_3Fe with bcc-Fe. This finding is also in agreement with experimental observations of this compound, known as the γ″-phase, in meteorite Fe–Ni alloys [2–4,47]. The γ″-phase is assumed to be metastable but very close to being truly stable [2]. Further, the calculations predict that the Fe_2Ni and Ni_2Fe compounds with the $C11_f$ structure are also relatively stable, and therefore could also form at low temperatures. To our knowledge, such compounds have not been observed experimentally as bulk phases or precipitates in Fe–Ni alloys. However, their stability revealed by the calculations allows us to suggest that such compounds could actually be found under certain experimental conditions. They could also form in core regions of grain boundaries or other lattice defects. A search for such compounds may deserve special efforts in the future.

Using the first-principles energy–volume functions calculated in this work, as well as some experimental data, we have developed a semi-empirical interatomic potential intended for atomistic simulations of the Fe–Ni system. Since the covalent component of bonding can play a significant role in this system, we have chosen an angular-dependent potential form, which we call ADP. This form is a generalization of the EAM method that additionally penalizes the total energy for dipole and quadrupole distortions of local atomic environments. An ADP potential set has been generated by first constructing potentials for pure Fe and pure Ni, followed by fitting Fe–Ni cross-interaction parameters to the energy–volume relations for some of the Fe–Ni compounds. Thus, while the Fe and Ni potentials are based

on both experimental and first-principles data, the cross-interaction potential is fit to first-principles data only.

The ADP potentials obtained reproduce a large variety of properties of Fe and Ni (Tables 3–5) and the formation energies of the Fe–Ni compounds (Fig. 1). The Fe and Ni potentials have certain advantages over existing EAM potentials for these metals. The improvement is due to the incorporation of first-principles data and the use of an angular-dependent potential form. The advantages of the ADP method are especially distinct for bcc-Fe, where the role of angular-dependent interactions is expected to be stronger than in Ni. It is the latter recognition that has always motivated the pursuit of angular-dependent potential forms for Fe, as well as for other bcc transition metals such as Nb, Mo, Ta and W [13,16–20,48–50]. Even if a regular EAM potential can provide the same or even better accuracy of fit to a particular property, when a large set of properties is considered, the ADP or other angular-dependent models are likely to lead to an overall better accuracy and should be more robust in atomistic simulations.

It must be emphasized, however, that neither our ADP nor any other Fe potential known to us correctly predict the phase transformations from bcc to fcc with temperature and then back to bcc before melting. These transformations are governed by an interplay between the thermal (i.e., associated with atomic vibrations) and magnetic contributions to the free energy [73] and can hardly be reproduced by traditional interatomic potentials. In particular, the stability of the bcc structure at low temperatures is due to its ferromagnetic ordering and not to the stronger cohesion as postulated by all potentials. Accordingly, the loss of stability of the bcc structure at elevated temperatures (>1185 K) is caused by the partial loss of its magnetic energy and not by competition between the thermal free energies of the bcc and fcc structures. One possible approach to modeling the phase transformations in Fe would be to include the magnetic energy explicitly using some semi-empirical model, for example by employing the Stoner model as it was suggested by Krasko [74]. An alternative way would be to make potential functions temperature-dependent in order to reflect the temperature-dependent contribution of the magnetic energy. Before one of such approaches is implemented in the future, atomistic simulations of Fe will have to be restricted to the bcc phase.

As demonstrated by Fig. 1, the ADP potential correctly reproduces the phase stability trends across the Fe–Ni system at 0 K. Both the ADP and LAPW calculations identify the same set of most stable compounds, including the experimentally observed $L1_2$–Ni_3Fe, the metastable $L1_0$–FeNi, and the previously unknown $C11_f$ compounds. Properties of the $L1_2$–Ni_3Fe phase *predicted* by the potential are in good agreement with experimental data (Table 6).

Since our ADP Fe remains bcc at all temperatures below the melting point, we cannot expect that the potential will correctly reproduce the experimental phase diagram. Nevertheless, exploratory grand-canonical Monte Carlo simulations have been performed in a few selected temperature-composition domains. The fcc-based solid solution (γ phase) has been found to exist at least up to 1600 K and to extend from pure Ni to about 70 at.% Fe. The Fe-rich part of the diagram is dominated by the bcc-α phase at all temperatures. This phase dissolves up to 10 at.% Ni, depending on the temperature. The Ni_3Fe-based γ'-phase has been observed below 800 K in equilibrium with either the γ or α phase. These features are in general agreement with the experimental phase diagram, except for the discontinuity of the γ-phase field on the Fe-rich side. Furthermore, low-temperature simulations have revealed the formation of both the $L1_0$–FeNi compound and the $C11_f$ phases, depending on the temperature, composition and initial conditions of the simulations. An exact reconstruction of the relevant low-temperature part of the phase diagram is computationally challenging and was not pursued in this work. We can conclude, however, that the ADP potentials developed in this work can be used for atomistic simulations of the α-phase at relatively low temperatures and the γ-phase at all temperatures as long as it contains at least 30 at.% of Ni.

This potential should be suitable for simulations of plastic deformation, fracture and other processes in model steels. In our ongoing work, it is applied to model the grain boundary structure and segregation in fcc Fe–Ni solid solutions at high temperatures. Simulations of the dislocation core structure and motion in bcc Fe are also in progress.

Acknowledgment

This work was supported by the Office of Naval Research through grant No. N00014-04-WX-2-0553.

Appendix

In the ADP method proposed in this work, the force f_i^γ acting on atom i in a Cartesian direction γ is given by

$$f_i^\gamma = \sum_{j\neq i} \left[\varphi_{ij}^\gamma + \psi_{ij}^\gamma\right],$$

where the summation runs over all neighbors j of atom i. Here,

$$\varphi_{ij}^\gamma = \Phi'_{s_i s_j}(r_{ij})\frac{r_{ij}^\gamma}{r_{ij}} + \left[F'_{s_i}(\bar{\rho}_i)\rho'_{s_j}(r_{ij}) + F'_{s_j}(\bar{\rho}_j)\rho'_{s_i}(r_{ij})\right]\frac{r_{ij}^\gamma}{r_{ij}}$$

is the standard force expression within regular EAM and

$$\psi_{ij}^{\gamma} = (\mu_i^{\gamma} - \mu_j^{\gamma})u_{s_i s_j}(r_{ij}) + \sum_{\alpha}\left(\mu_i^{\alpha} - \mu_j^{\alpha}\right)u'_{s_i s_j}(r_{ik})\frac{r_{ij}^{\gamma} r_{ij}^{\alpha}}{r_{ij}} + 2\sum_{\alpha}\left(\lambda_i^{\alpha\gamma} + \lambda_j^{\alpha\gamma}\right)w_{s_i s_j}(r_{ij})r_{ij}^{\alpha} + \sum_{\alpha,\beta}\left(\lambda_i^{\alpha\beta} + \lambda_j^{\alpha\beta}\right)w'_{s_i s_j}(r_{ij})\frac{r_{ij}^{\alpha} r_{ij}^{\beta} r_{ij}^{\gamma}}{r_{ij}} + \frac{1}{3}(v_i + v_j)\left[w'_{s_i s_j}(r_{ij})r_{ij} + 2w_{s_i s_j}(r_{ij})\right]r_{ij}^{\gamma}$$

is the contribution of the angular-dependent forces. In these expressions, μ_i^{α} and $\lambda_i^{\alpha\beta}$ are the dipole and quadrupole tensors defined by Eqs. (3) and (4), respectively, and v_i is given by Eq. (5). The Greek superscripts denote components of vectors and tensors relative to a orthonormal Cartesian coordinate system. The prime signifies differentiation with respect to the interatomic distance r_{ij}.

References

[1] Massalski TB, editor. Binary alloy phase diagrams. Materials Park (OH): ASM; 1986.
[2] Howald RA. Metall Mater Trans A 2003;34:1759.
[3] Reuter KB, Williams DB, Goldstein JI. Metall Trans A 1989;20:719.
[4] Yang CW, Williams DB, Goldstein JI. J Phase Equilib 1996;17:522.
[5] Grujicic M, Zhou XW. Mater Sci Eng A 1995;190:87.
[6] Meyer R, Entel P. Phys Rev B 1998;57:5140.
[7] Entel P, Meyer R, Kadau K, Herper HC, Hoffmann E. Eur Phys J B 1998;5:379.
[8] Daw MS, Baskes MI. Phys Rev B 1984;29:6443.
[9] Harrison RJ, Voter AF, Chen SP. In: Vitek V, Srolovitz DJ, editors. Atomistic simulation of materials: beyond pair potentials. New York (NY): Plenum Press; 1989. p. 219–22.
[10] Johnson RA, Oh DJ. J Mater Res 1989;4:1195.
[11] Guellil AM, Adams JB. J Mater Res 1992;7:639.
[12] Ackland GJ, Bacon DJ, Calder AF, Harry T. Philos Mag A 1997;75:713.
[13] Simonelli G, Pasianot R, Savino EJ. Phys Status Solidi (b) 2000;217:747.
[14] Mendelev MI, Han S, Srolovitz DJ, Ackland GJ, Sun DY, Asta M. Philos Mag 2003;83:3977.
[15] Wallenius J, Olsson P, Lagerstedt C, Sandberg N, Chakarova R, Pontikis V. Phys Rev B 2004;69:094103.
[16] Baskes MI. Phys Rev B 1992;46:2727.
[17] Lee BJ, Baskes MI, Kim H, Cho YK. Phys Rev B 2001;64:184102.
[18] Pasianot R, Farkas D, Savino EJ. Phys Rev B 1991;43:6952.
[19] Simonelli G, Pasianot R, Savino EJ. Phys Rev B 1994;50:727.
[20] Simonelli G, Pasianot R, Savino EJ. Phys Rev B 1997;55:5570.
[21] Ercolessi F, Adams JB. Europhys Lett 1994;26:583.
[22] Mishin Y, Farkas D, Mehl MJ, Papaconstantopoulos DA. Phys Rev B 1999;59:3393.
[23] Baskes MI, Asta M, Srinivasan SG. Philos Mag A 2001;81:991.
[24] Mishin Y, Mehl MJ, Papaconstantopoulos DA, Voter AF, Kress JD. Phys Rev B 2001;63:224106.
[25] Mishin Y, Mehl MJ, Papaconstantopoulos DA. Phys Rev B 2002;65:224114.
[26] Li Y, Siegel DJ, Adams JB, Liu XY. Phys Rev B 2003;67:125101.
[27] Zope RR, Mishin Y. Phys Rev B 2003;68:024102.
[28] Mishin Y. Acta Mater 2004;52:1451.
[29] Wei S-H, Krakauer H. Phys Rev Lett 1985;55:1200.
[30] Andersen OK. Phys Rev B 1975;12:3060.
[31] Koelling DD, Harmon BN. J Phys C 1977;10:3107.
[32] Singh D. Phys Rev B 1991;43:6388.
[33] Perdew JP, Chevary JA, Vosko SH, Jackson KA, Pederson MR, Singh DJ, et al. Phys Rev B 1992;46:6671.
[34] von Barth U, Hedin L. J Phys C 1972;5:1629.
[35] Hohenberg P, Kohn W. Phys Rev 1964;136:B864.
[36] Kohn W, Sham LJ. Phys Rev 1965;140:A1133.
[37] Wang CS, Klein BM, Krakauer H. Phys Rev Lett 1985;54:1852.
[38] Singh DJ, Pickett WE, Krakauer H. Phys Rev B 1991;43:11628.
[39] Gillan MJ. J Phys Condens Matter 1989;1:689.
[40] Mehl MJ. Phys Rev B 2000;61:1654.
[41] Mehl MJ. Phys Rev B 1993;47:2493.
[42] Birch F. J Geophys Res 1978;83:1257.
[43] Herper HC, Hoffmann E, Entel P. Phys Rev B 1999;60:3839.
[44] Friak M, Sob M, Vitek V. Phys Rev B 2001;63:052405.
[45] Clatterbuck DM, Chrzan DC, Morris JW. Acta Mater 2003;51:2271.
[46] Jiang DE, Carter EA. Phys Rev B 2003;67:214103.
[47] Villars P, Calvert LD. Pearson's handbook of crystallographic data for intermetallic phases vol. 3. Metals Park (OH): ASM International; 1996.
[48] Baskes MI. Phys Rev Lett 1987;59:2666.
[49] Baskes MI, Nelson JS, Wright AF. Phys Rev B 1989;40:6085.
[50] Baskes MI, Johnson RA. Modell Simul Mater Sci Eng 1994;2:147.
[51] Rose JH, Smith JR, Guinea F, Ferrante J. Phys Rev B 1984;29:2963.
[52] Voter AF. Intermetallic compounds, vol. 1. New York (NY): John Wiley; 1994. p. 77 [chapter 4].
[53] Kittel C. Introduction to solid state physics. New York (NY): Wiley–Interscience; 1986.
[54] Schepper LD, Segers D, Dorikens-Vapaert L, Dorikens M, Knuyt G, Stals L, et al. Phys Rev B 1983;27:5257.
[55] Vehanen A, Hautojärvi P, Johnsson J, Yli-Kaupilla J, Moser P. Phys Rev B 1982;25:762.
[56] Lübbenhusen M, Mehrer H. Acta Metall Mater 1990;38:283.
[57] Seeger A. Phys Status Solidi A 1998;167:289.
[58] Domain C, Becquart C. Phys Rev B 2002;65:024103.
[59] Fu CC, Willaime F. Phys Rev Lett 2004;92:175503.
[60] Fu CC, Torre JD, Willaime F, Bocquet J-L, Barbu A. Nat Mater 2005;4:68.
[61] Jónsson H, Mills KW, Jacobsen G. In: Berne BJ, Ciccotti G, Coker DF, editors. Classical and quantum dynamics in condensed phase simulations. Singapore: World Scientific; 1998.
[62] Henkelman G, Johannesson G, Jónsson H. Theoretical methods in condensed phase chemistry. In: Schwartz SD, editor. Progress in theoretical chemistry and physics, vol. 5. Dordrecht: Kluwer Academic Publishers; 2000 [chapter 10].
[63] Mehl MJ, Papaconstantopoulos DA. In: Yip S, editor. Handbook of materials modeling.
[64] Yan JA, Wang CY, Wang SY. Phys Rev B 2004;70:174105.
[65] Metals: phonon states, electron states, and Fermi surfaces, vol. 13, Landolt-Bornstein, New Series, Group III, Springer, Berlin, 1981, Part a.
[66] Schaefer H-E, Gugelmeier R, Schmolz M, Seeger A. Mater Sci Forum 1987;15–18:111.
[67] Balluffi RW. J Nucl Mater 1978;69–70:240.
[68] Peterson NL. J Nucl Mater 1978;69–70:3.
[69] Murr LE. Interfacial phenomena in metals and alloys. Reading, MA: Addison-Wesley; 1975.

[70] Zimmermann JA, Gao HJ, Abraham FF. Modell Simul Mater Sci Eng 2000;8:103.
[71] Tyson WR, Miller WA. Surf Sci 1977;62:267.
[72] Mittendorfer F, Eichler A, Hafner J. Surf Sci 1999;423:1.
[73] Nishizawa T. J Phase Equilib 1995;16:379.
[74] Krasko GL. J Appl Phys 1996;79:4682.
[75] Hirth JP, Lothe J. Theory of dislocations. 2nd ed. New York (NY): John Wiley; 1982.
[76] Touloukian YS, Kirby RK, Taylor RE, Desai PD, editors. Thermal expansion: metallic elements and alloys, vol. 12. New York (NY): Plenum; 1975.
[77] Simmons G, Wang H. Single crystal elastic constants and calculated aggregate properties. Cambridge (MA): MIT Press; 1977.
[78] Lutts Gielen A, Gielen PM. Phys Status Solidi 1970;41: K81.